Journal of Materials Chemistry A

ROYAL SOCIETY OF CHEMISTRY

PAPER

View Article Online
View Journal | View Issue

Cite this: J. Mater. Chem. A, 2023, 11, 6226

Adjusting the band gap of $CsPbBr_{3-y}X_y$ (X = Cl, I) for optimal interfacial charge transfer and enhanced photocatalytic hydrogen generation†

Marija Knezevic, [a] Vien-Duong Quach, [a] Isabelle Lampre, [a] Marie Erard,[a] Pascal Pernot,[a] David Berardan, [b] Christophe Colbeau-Justin[a] and Mohamed Nawfal Ghazzal *[a]

Metal halide perovskites (MHPs, $CsPbX_3$: X = Cl, Br, I) demonstrate high photogenerated charge-carrier production and mobility, which makes them promising candidates for photocatalysis. In this work, we investigated how adjusting the band gap energy of MHPs at room temperature by anion exchange ($CsPbBr_{3-y}X_y$: X = Cl, Br, I) leads to optimal interfacial electron transfer from $CsPbBr_{3-y}X_y$ to TiO_2 by means of transient absorption spectroscopy (TAS), time-resolved photoluminescence (TRPL), and time-resolved microwave conductivity (TRMC). We found that the formation of indirect excitons at the MHPs/TiO_2 interface results in slower charge-carrier relaxation, which is essential for photocatalysis. The substitution of bromide with chloride reduces the trapping states (healing effect), which favors charge-carrier relaxation to the ground state and leads to higher charge recombination and lower photocatalytic activity. The iodine, on its side, acts as a hole trapper proposing an optimal band gap facilitating fast charge injection in the TiO_2. The charge-carrier injection from one material to another suppresses recombination, leading to impressive H_2 generation.

Received 21st December 2022
Accepted 24th February 2023

DOI: 10.1039/d2ta09920a

rsc.li/materials-a

Introduction

The recent energy crisis and constant energy demand growth have been prompting the need for new sustainable energy sources. Metal-halide perovskites (MHPs, $CsPbX_3$: X = Cl, Br, I), known for their extraordinary light-harvesting capacity and charge-carrier dynamics[1] (*i.e.*, high photogenerated charge-carrier production and mobility), could play an important role in resolving the current energy-matter. MHPs have been extensively investigated in the field of optoelectronic devices and solar cells, reaching a record of energy conversion efficiency of up to 32.5% for perovskite-silicon tandem solar cells, and 25.7% for single-junction perovskite solar cells.[2] Due to their impressive photophysical properties, MHPs are a valid candidate for photocatalysis. However, their inherent instability upon exposure to moisture, polar solvents, and UV irradiation, enhances their interactions with CO_2, O_2, and H_2O, resulting in anodic corrosion, *i.e.* PbO formation, decelerating their immediate application in photocatalysis.[3]

Therefore, significant attention has been paid to MHPs encapsulation with non-toxic and stable materials. MHPs encapsulation has been beneficial for CO_2 photocatalytic reduction when coupled to graphdiyne (GDY),[4] graphene oxide,[5] titanium dioxide,[6] boron imidazolate frameworks (BIFs)[7] zeolite,[8] poly(3-hexylthiophene-2,5-diyl) (P3HT) polymer,[9] fullerene,[10] MXene nanosheets,[11] and porous g-C_3N_4 (PCN),[12] while hydrogen production was improved by encapsulation in polymers such as polyaniline (PANI), and metal–organic-frameworks derived Co_3O_4/N-doped C core/shell composite.[13,14] MHPs are also capable of singlet oxygen generation through energy transfer during methyl orange photocatalytic degradation when coated with stable and inert SiO_2.[15] Furthermore, coupling with metallic co-catalysts such as Ni(tpy)[16] and $Re(CO)_3Br(dcbpy)$ (dcbpy = 4,4′-dicarboxy-2,2′-bipyridine)[17] complex molecules improves photocatalytic efficiency of CO_2 reduction, *e.g.*, Ni(tpy) can act as the electron sink, preventing electron–hole recombination in $CsPbBr_3$ nanocrystals (NCs). In general, heterojunctions improve the efficiency of the photogenerated charge carriers (*i.e.*, electron–hole separation) and the CO_2 capture. It is worth noting that one must consider the oxidation of carbon-based materials to CO_2 and CO during the photocatalytic reaction since it could influence the yield of CO.[18] Moreover, it is possible to maximize MHPs efficiency by using non-polar solvents *e.g.*, mixed metal halide perovskite $CsPb(Br_{0.5}/Cl_{0.5})_3$ demonstrated the effective reduction of CO_2 from ethyl acetate saturated solution.[19]

[a]Institut de Chimie Physique, UMR 8000 CNRS, Université Paris-Saclay, F-91405 Orsay, France. E-mail: mohamed-nawfal.ghazzal@universite-paris-saclay.fr
[b]Institut de Chimie Moléculaire et des Matériaux d'Orsay, UMR 8182 CNRS, Université Paris-Saclay, F-91405 Orsay, France

† Electronic supplementary information (ESI) available. See DOI: https://doi.org/10.1039/d2ta09920a

The growing interest of the photocatalytic community for MHPs has led to the development of different strategies to promote the photoelectronic and photocatalytic performance of MHPs, including selective control of MHP synthetic procedures, offering great versatility in morphology control, and electronic band gap engineering. Such an approach considers the replacement of long-chain oleic acid with either short-chain glycine or methyl acetate, directly ameliorating photocatalytic activity in CO_2 reduction, due to the large available surface-active area.[20,21] The latter could also be improved through multifaceted morphology control, eventually resulting in enhanced photocatalytic efficiency.[22] In general, the MHPs band gap modification has been typically introduced by anion substitution reaction and metallic doping *e.g.* Fe(II), Co(II), Mn(II), and Zn(II).[23–26] Nevertheless, the relationship between adjusting the band gap of MHP, interfacial charge lifetime, and photocatalytic activity has been scarcely investigated.

In this work, we adjusted interfacial charge transfer and lifetime by constructing tunable band gap energy of a heterojunction between MHP and TiO_2. The band gap of MHP was controlled by post-anion substitution at room temperature. Then, we successfully encapsulated MHPs by sol–gel coating, constructing stable MHPs covered by TiO_2 overlayer. The lifetime of photogenerated charges was followed at a variable time scale (from fs to μs) using transient absorption spectroscopy (TAS, fs), time-resolved photoluminescence (TRPL, ns), and time-resolved microwave conductivity (TRMC, μs). The optimal band gap configuration exhibits highly efficient charge injection and demonstrates stable photocatalytic hydrogen production in an aqueous solution, compared to solely MHPs. We found that chloride substitution enhances photoluminescence in the Br/Cl mixed halide perovskites, whereas iodide is the best candidate to promote photocatalytic H_2 generation.

Experimental section

Synthetic procedures

Synthesis of $CsPbBr_3$ NCs. $CsPbBr_3$ nanocrystals were synthesized by the hot-injection method at 200 °C following the previously reported procedures.[27,28]

Sol–gel synthesis of $CsPbBr_3$ perovskites covered by TiO_2 overlayer nanostructure ($CsPbBr_3$@TiO_2)

Titanium isopropoxide (TTiP, 20 μL) was dissolved in 1 mL of hexane and added dropwise in 10 mL colloidal solution of $CsPbBr_3$ in hexane (1 mg mL^{-1}) under vigorous stirring. The solution was aged for 3 h under stirring at ambient temperature. Then, the obtained nanoparticles were recovered by centrifugation and dried overnight at 80 °C. The final MHP@TiO_2 nanomaterials were calcinated at 300 °C under air for 2 h. The same procedure was employed for titanium diisopropoxide bis(acetylacetonate) (TAA), titanium(IV) butoxide (TBOT), and titanium(IV) chloride ($TiCl_4$).

$PbCl_2$ (14 mM) stock solution. $PbCl_2$, oleylamine (OAm, 1.2 mL), oleic acid (OAc, 0.8 mL), trioctylphosphine (TOP, 1 mL), and octadecene (ODE, 18 mL) were mixed and heated at 140 °C until complete dissolution of $PbCl_2$.

PbI_2 (14 mM) stock solution. PbI_2, OAm (0.6 mL), OAc (0.4 mL), and ODE (20 mL) were mixed and heated at 120 °C until the complete dissolution of PbI_2.

Anion exchange reactions. In previously prepared $CsPbBr_3$ or $CsPbBr_3$@TiO_2 nanocrystals (10 mL, 1 mg mL^{-1}) different amounts of PbX_2 solution were added under vigorous stirring, for 1 h, at room temperature. Subsequently, precipitates were collected by centrifugation, washed with hexane to remove the excess of the remaining PbX_2, and dried at 80 °C.

Synthesis of TiO_2 thin films. TiO_2 thin films were synthesized following the previously reported procedure for an acid-catalyzed sol–gel process at room temperature.[29] TTiP (10 mL) was dissolved in absolute ethanol (50 mL) under stirring. The hydrolysis of the precursor is catalyzed by adding 1.3 mL of HCl. The sol is stirred for 30 min, and then a mixture of water (0.6 mL) and absolute ethanol (50 mL) was added dropwise, followed by stirring for 2 h, under an ambient atmosphere. The TiO_2 films were prepared by spin-coating 1 mL of the as prepared sol solution at 2000 rpm. Subsequently, the substrates were dried at 70 °C for 2 h, and then calcined at 500 °C with the heating rate of 1 °C min^{-1} for 2 h.

Characterization

Diffusion reflectance spectra (DRS) were recorded using UV-vis-NIR Cary 5000 spectrophotometer (Agilent Technologies), equipped with an integrating sphere for diffuse and total reflection measurements. The maximum reflectance was set to 100% using $BaSO_4$ as a reference in the 200 to 1100 nm wavelength range.

The photoluminescence (PL) emission spectra of colloidal MHPs in hexane were recorded using Fluorolog 3 HORIBA fluorimeter. All samples were excited at 400 nm (5 nm slit), and emission was monitored in the 420 to 700 nm range (1 nm slit).

X-ray diffraction (XRD) measurements were carried out by room temperature powder X-ray diffraction (P-XRD). Patterns were recorded by a Panalytical X'Pert diffractometer with a Ge (111) incident monochromator (Cu Kα radiation) and an X'cellerator detector.

Transmission electron microscopy (TEM, JEOL JEM 2100Plus, operating at 200 kV) was used to study the morphology of samples. The samples were ground, dispersed in hexane, and then drop-casted on carbon-coated copper grids. The grids were dried at ambient atmosphere before the measurements. The size of synthesized nanostructures was determined by ImageJ software.

Scanning transmission electron microscopy (STEM) experiments were performed on a Titan^3 G2 80-300 microscope, operating at 200 kV equipped with a high angle annular dark field (HAADF) detector and an extra-high-brightness field emission gun (XFEG) for energy-dispersive X-ray spectroscopy (EDS) mapping.

Femtosecond transient-absorption spectroscopy TAS spectra of $CsPbBr_{3-y}X_y$ and $CsPbBr_{3-y}X_y$/TiO_2 thin films were recorded with a homemade pump–probe set-up based on a commercial

amplified titanium sapphire laser (Amplitude Laser) that delivered pulses (780 nm, 110 fs) at a repetition rate of 1 kHz. The pump beam (390 nm) was generated using 90% of the fundamental beam by second harmonic generation in a 2 mm thick BBO crystal. The 10% left of the fundamental beam was used to generate a white light continuum (WLC) (400–800 nm) in a rotating fused silica plate. A broadband beam splitter was then used to divide the WLC into probe and reference beams. The probe and reference beams were transported and focused after attenuation on the entrance slit of a polychromator equipped with a charge-coupled device (CCD) camera (Princeton Instruments). The resolution of the system was about 200 fs. The 390 nm pump pulses were focused on the samples to a diameter of 780 ± 50 μm, and their energy was adjusted to vary the fluence (209 and 418 μJ cm^{-2}). The time-resolved spectra were recorded from 430 to 650 nm and corrected for the group velocity dispersion. The spectro-kinetics data were then analyzed by global target analysis with sequential models with increasing lifetimes, using SK-Ana software.[30–32]

Time-resolved laser scanning time-correlated single photon counting (TCSPC) microscopy was performed with a homemade setup based on a TE2000 Nikon microscope equipped with a 60× 1.2 NA water immersion objective. The pulsed excitation source was a LDH 440 nm pulsed diode (80 ps FWHM, 20 MHz of repetition rate, PicoQuant). The emitted luminescence was selected with the appropriate filter (480 +/− 30 nm or 535 +/− 20 nm) and detected by a MCP-PMT (Hamamatsu), which is connected to the PicoHarp 300 TCSPC module (PicoQuant). Lifetime measurements were analyzed by the Pico-quant SymPhoTime64 software (v5.3.2).[33]

Time-resolved microwave conductivity (TRMC) signals were recorded using a nanosecond laser system (EKSPLA) integrating a Nd:YAG laser and an optical parametric oscillator (OPO) which delivers 8 ns pulses at a tunable wavelength from 225 to 2000 nm and a repetition rate of 10 Hz.[34,35] All TRMC measurements were performed at the excitation wavelength of 360 and 440 nm, with a laser energy of 1.3 mJ and 2.6 mJ, respectively. The incident microwave was generated using a 30 GHz Gunn diode.

Photoelectrochemical (PEC) measurements were carried out in a quartz photoelectrochemical cell with a three-electrode setup, involving a Pt disk counter electrode, a non-aqueous reference electrode Ag|($AgNO_3$ 0.01 M, (Bu_4N)(PF_6) 0.1 M in CH_3CN), and a working electrode. The working electrodes were prepared by depositing MHPs previously dispersed in hexane on fluorine-doped tin oxide-coated glass (FTO); the amount of deposited MHPs and the surface area of the FTO slides remained unchanged for all samples. Amperometric transient photocurrent (TPC) was recorded at a bias voltage of 0.7 V (*vs.* ref), under 20 seconds solar light illumination delivered by solar light stimulator AM 1.5G, using (Bu_4N)(PF_6) 0.1 M in a mixture of CH_3OH : CH_3CN (1 : 3 v/v) as a supporting electrolyte. The electrolyte was replaced by (Bu_4N)(PF_6) 0.1 M in dichloromethane (DCM) for cyclic voltammetry (CV) measurements. The formal potential of the non-aqueous reference electrode $Ag|Ag^+$ was calibrated by adding 2 mM ferrocene/ferrocenium (Fc/Fc^+) as an internal standard at the end of measurements. All measurements were performed on PGSTAT101 Metrohm Autolab potentiostat.

Photocatalytic evolution of H_2. In order to assess the photocatalytic activity of MHP@TiO_2 nanostructures, in a quartz reactor, 3 mg of the photocatalyst was dispersed in 3 mL of the aqueous solution of 25 vol% glycerol and degassed under a continuous flow of Ar gas (>99%, Air liquid) to remove dissolved oxygen. The samples were irradiated using an Oriel 300 W Xenon lamp with an infrared water filter for 3 h under stirring, and the gas sample was analyzed every 30 min by gas chromatography (GC) (Chemlys gas chromatographer).

Results and discussion

Synthesis and physicochemical characterization of $CsPbBr_{3-y}X_y$ and $CsPbBr_{3-y}X_y$@TiO_2 nanopowders

Cesium-lead bromide ($CsPbBr_3$) nanoparticles are synthesized by a hot injection colloidal synthesis at 200 °C.[27,28] The post-anion exchange reactions are performed by adjusting the amount of lead halide salts (PbX_2) in $CsPbBr_3$ colloidal solution at room temperature, yielding $CsPbBr_{1.65}Cl_{1.35}$, $CsPbBr_{1.95}Cl_{1.05}$, $CsPbBr_{1.95}I_{1.05}$, and $CsPbBr_{1.65}I_{1.35}$, where Br/X represents their molar ratio in crude solution (Fig. 1a). The post-anion substitution, which differs from the usually reported one-pot hot injection synthesis process,[36] took up to several minutes (under stirring) to reach an equilibrium, and allow efficient and non-reversible anion insertion into the crystalline structure. The anion exchange enables a fine band gap tuning all over the visible range, as demonstrated by the red and blue shift observed in the UV-visible spectra (Fig. 1b). The PL spectra of such exchanged nanocrystalline materials are adequately shifted with respect to the optical absorption spectra (Fig. 1c). We estimated the optical band gap energy to vary from 2.95 eV ($CsPbCl_3$) to 2.06 eV ($CsPbBr_{1.65}I_{1.35}$) using Kubelka–Munk modified function (Fig. 1c and Table S1†). Luminescent properties of colloidal MHPs in hexane were explored under UV light excitation (360 nm), demonstrating the emission from blue ($CsPbBr_{1.65}Cl_{1.35}$), green ($CsPbBr_3$) to yellow ($CsPbBr_{1.65}I_{1.35}$) (Fig. 1c, inset). The prevalence of iodide dramatically reduces the PL intensity of colloidal NCs, which almost completely vanished when samples were precipitated and dried (not shown), demonstrating the crucial role of the ligand/solvent environment for defect passivation.

Introducing chloride and iodide in the structure leads to a shift in the valence band maximum (VBM) and conduction band minimum (CBM), although halide contribution is more significant in the valence band, consisting of either 3p, 4p, or 5p orbitals of chloride, bromide, and iodide, respectively.[37] We determined VBM and CBM of MHPs by cyclic voltammetry. The charge transfer between $CsPbBr_3$ and FTO conductive glass at working electrodes was reflected by anodic (A_2) and cathodic (C_1) peaks, respectively. The potential gap between anodic and cathodic peaks reveals the so-called quasi-particle band gap (E_g^{qp}) and its value should be relatively close to the optical band gap (E_g^{opt}) extracted from the Kubelka–Munk function.[38] The irreversible voltammogram of $CsPbBr_3$ was observed as a negative-sweeping potential scan from 0.5 (V *vs.* SHE) up to −1.63

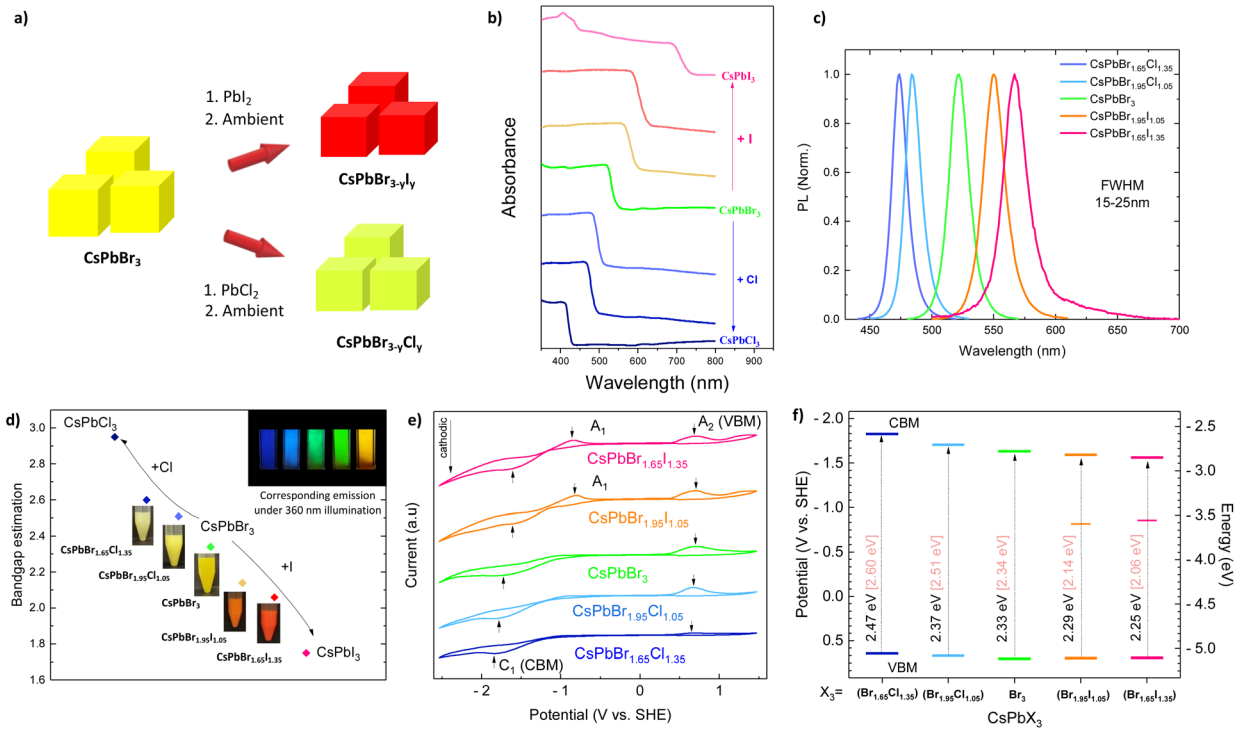

Fig. 1 (a) Schematic representation of $CsPbBr_{3-y}X_y$ and $CsPbBr_{3-y}X_y$ (X = Cl, I) synthesis; (b) absorption spectra of solid $CsPbBr_{3-y}X_y$ MHPs, (c) PL spectra of colloidal $CsPbBr_{3-y}X_y$ MHPs, and (d) Kubelka–Munk optical band gap estimation of $CsPbBr_{3-y}X_y$ MHPs, inset in (d) photographs of $CsPbBr_{1.65}Cl_{1.35}$, $CsPbBr_{1.35}Cl_{1.05}$, $CsPbBr_3$, $CsPbBr_{1.35}I_{1.05}$, and $CsPbBr_{1.65}I_{1.35}$ colloidal solution in hexane. (e) Cyclic voltammograms of $CsPbBr_{3-y}X_y$ recorded at 50 mV s^{-1} in a solution of 100 mM $(Bu_4N)(PF_6)$ in DCM showing oxidation (A_2) and reduction (C_1) peaks, A_1 peaks were marked out for iodide perovskites. (f) Energy band edge diagram of MHPs deduced from (e). Electrochemical band gap values (E_g^{qp}, black) were compared to optical ones ($E_{g,}^{opt}$pale pink).

(C_1) (V *vs.* SHE), with the continuous current increase due to further reduction of NCs. Upon the reverse of the potential scan, oxidation of MHPs occurred and produced an anodic wave; we recorded an oxidation peak (A_2) at 0.70 (V *vs.* SHE). The irreversibility could be ascribed to the partial degradation of MHPs after charge transfer (Fig. S1a†).[38,39] Fig. 1e depicts cyclic voltammograms of the mix-halide MHPs, including $CsPb(Br_{1.65}Cl_{1.35})$, $CsPb(Br_{1.95}Cl_{1.05})$, $CsPb(Br_{1.95}I_{1.05})$, $CsPb(Br_{1.65}I_{1.35})$ in comparison with $CsPbBr_3$. In addition to anodic (A_2) and cathodic (C_1) peaks, we observed an additional peak A_1 in the case of iodide-substituted perovskites. This can be attributed to trap-to-band transition.[40] The potential gap between the peaks was similar to the optical band gap estimation (Fig. 1f).

The hot-injection synthesis yields orthorhombic $CsPbBr_3$ NCs with an average size of 18 nm (Fig. 2a and S2†). A room-temperature anion substitution provides well-crystallized metal-halide perovskites, where both Br/Cl and Br/I halogen mixed perovskites keep the same orthorhombic crystal structure as pristine $CsPbBr_3$ (Fig. 2b). The lattice parameters, space group, and crystal symmetry of $CsPbBr_{3-y}X_y$ (X = Cl, I) are given in Table S2.† The evolution of the average unit cell spacing was compatible with anion substitution, either iodide or chloride, in which the partial substitution exhibits intermediate cell parameters between those of the parent particles. The synthesis of pure $CsPbI_3$ results in the quick transformation from dark to a yellow orthorhombic non-perovskite phase, while $CsPbCl_3$ crystallizes in a tetragonal phase (Fig. S3†). The anion substitution rate was estimated by STEM-EDS mapping (Fig. 2c–e and S4†), revealing easier chloride penetration *e.g.*, $CsPbBr_{1.95}X_{1.05}$ substitution yields $CsPbBr_{2.2}Cl_{0.6}$, and $CsPb_{1.2}Br_2I_{0.16}$, with an average particle size of 25 and 22 nm, respectively, similar to the size of $CsPbBr_3$ NCs (Fig. 2c–e). An easier penetration of chloride is attributed to the smaller atomic size of chloride compared to iodide, allowing facile diffusion in $CsPbBr_3$ nanocubes. It is worth mentioning that during the STEM and TEM analysis, the long beam exposure induces the degradation of MHPs and leads to the formation of lead nanoparticles (dots at the surface).[41]

Considering MHPs stability issues and interfacial charge separation, we coated MHPs with a thin TiO_2 overlayer (Fig. 3a). We elaborated MHPs coating with different TiO_2 precursors (*e.g.*, TAA, TTiP, TBOT, and $TiCl_4$). We found that TTiP and TBOT are homogeneously coated on the MHP surface (Fig. 3 and S5†), whereas TAA altered the cubic particle morphology. We could not observe a distinctive overlayer when $TiCl_4$ was used as a precursor. Moreover, $TiCl_4$ easily triggers Cl substitution, which could be observed as a blue-shifted absorption spectral line (Fig. S6†). We performed all the experiments with TTiP, due to its optimal hydrolysis reaction and better NCs dispersion. The sol–gel process enables obtaining perovskite nanoparticles covered by a thin TiO_x layer. However, we have to avoid MHPs dispersion in the solution by ultrasonication before

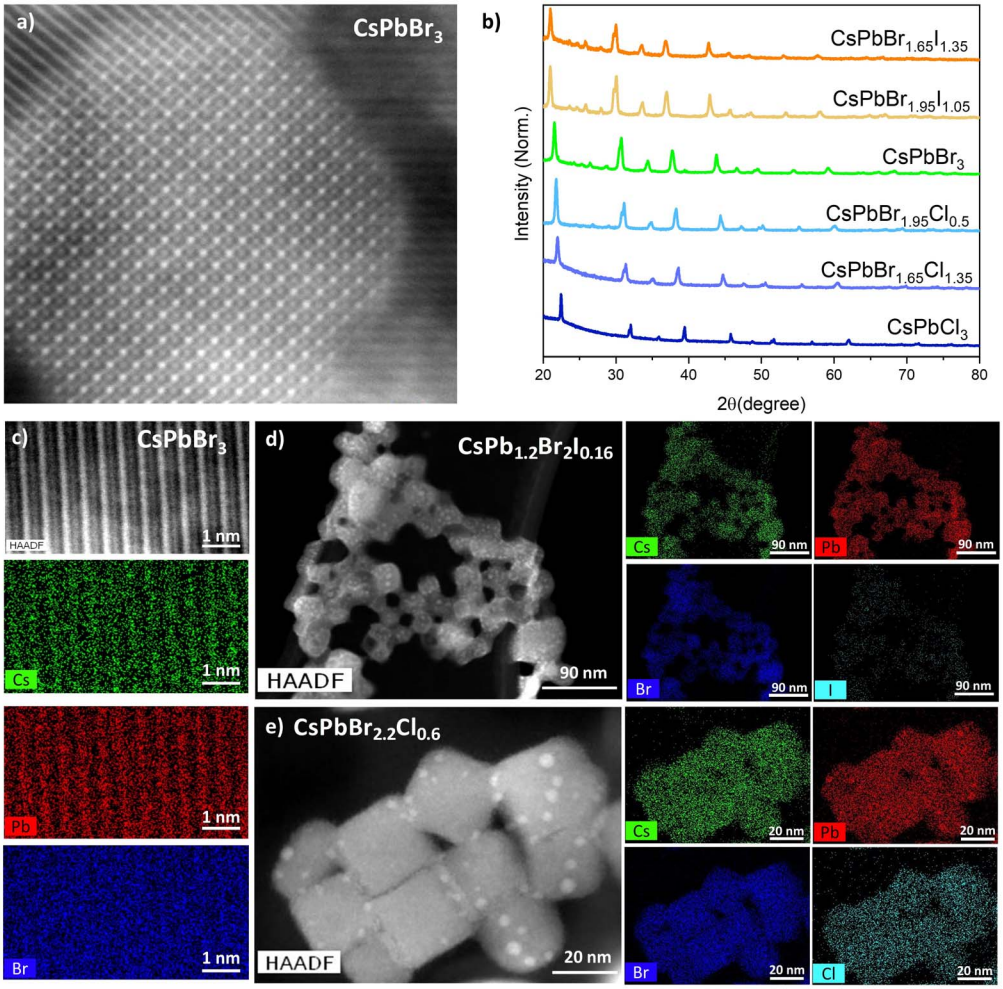

Fig. 2 (a) XRD patterns of $CsPbBr_{3-y}X_y$ (X = Cl, I); (b) STEM image of $CsPbBr_3$; STEM-EDS mapping of (c) $CsPbBr_3$, (d) $CsPbBr_{1.95}I_{1.05}$, and (e) $CsPbBr_{1.95}Cl_{1.05}$.

the coating procedure. Indeed, ultrasonication should be avoided since the perovskites are easily dissociated in solution (destroyed). Therefore, the obtained material is an agglomerate-like perovskite fully covered by a TiO_x layer (labeled $CsPbBr_3@TiO_x$) (Fig. 3b, c and S7†).

As synthesized $CsPbBr_3@TiO_x$ NCs were further calcined at 300 °C to obtain a crystalline TiO_2 overlayer ($CsPbBr_3@TiO_2$) (Fig. 3d). STEM-EDS mapping showed a homogenous distribution of the Ti and O signal all over the Cs, Pb, and Br, indicating the successful deposition of TiO_2 layer, which is in agreement with the TEM images, and EDS mapping (Fig. 3e and S8†). The obtained $CsPbBr_3@TiO_2$ nanostructures retained their optical properties and orthorhombic crystal structure upon thermal treatment, as evidenced by XRD (Fig. S9†). The optical properties of $CsPbBr_3$ and $CsPbBr_3@TiO_2$ exhibit similar behavior as shown in Fig. S10.† The composite nanostructure shows a shift of its absorption edge to 533 nm, with an enlarged (shoulder-like) absorption probably due to carbon residues.[42] The optical band gap of $CsPbBr_3$ and $CsPbBr_3@TiO_2$ is estimated using the Kubelka–Munk function to be similar to 2.34 eV and 2.35 eV, respectively. The TiO_2 porous layer allows anion diffusion resulting in a band gap tuning (Fig. 3a and S11†). The UV-vis spectra show gradual redshift and blueshift when Br is substituted by I and Cl, respectively (Fig. S11†). We have performed gradual anion exchange substitution with an increasing amount of the adequate precursor (PbI_2 and $PbCl_2$), and we have observed uniform red and blue shifts (Fig. S11†). At higher concentrations of PbI_2, no significant change in the absorption spectrum was observed after $CsPbBr_{1.44}I_{1.56}@TiO_2$, indicating a maximum ion substitution is reached. The emission spectra of $CsPbBr_{3-y}X_y@TiO_2$ (X = Cl, I) demonstrate homogenous blue- and redshifts (Fig. S12†). However, photoluminescence intensity is significantly quenched compared to the non-coated MHPs, having been completely diminished after $CsPbBr_{1.95}I_{1.05}@TiO_2$. STEM-EDS mapping of anion exchanged $CsPbBr_{1.95}Cl_{1.05}@TiO_2$ and $CsPbBr_{1.95}I_{1.05}@TiO_2$ shows a homogeneous distribution of bromide, iodide, and chloride, and well-covered MHPs with TiO_2 overlayer (Fig. S13–S16†). It is worth noting that upon calcination, we observe a growth of the TiO_2 layer due to crystallization, resulting in a thicker overlayer than the amorphous TiO_x. As prepared $MHPs@TiO_2$ were investigated for photocatalytic activity.

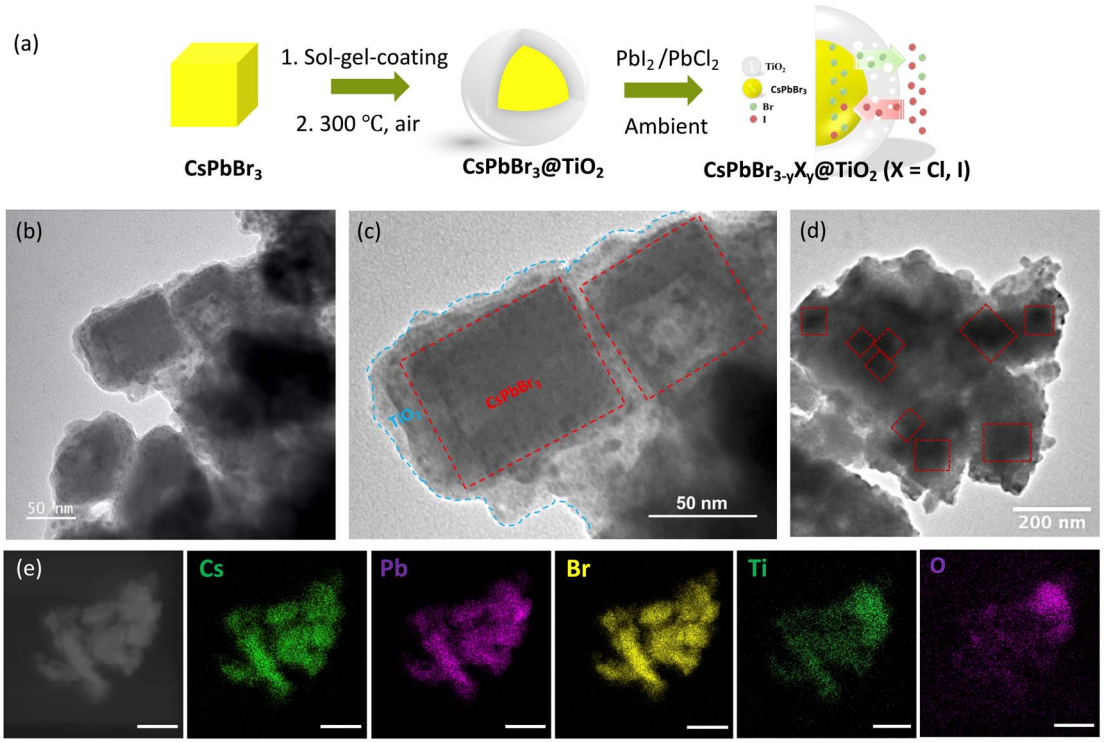

Fig. 3 (a) Schematic representation of the sol–gel synthesis of $CsPbBr_3$ covered by TiO_x (TTiP) overlayer ($CsPbBr_3@TiO_x$), (b and c) TEM images of $CsPbBr_3@TiO_x$, (d) TEM and (e) EDS mapping images of $CsPbBr_3@TiO_2$ upon calcination at 300 °C. The scale bar corresponds to 300 nm.

Femtosecond transient absorption spectra of $CsPbBr_{3-y}X_y$ and $CsPbBr_{3-y}X_y/TiO_2$ (X = Cl, I) thin films

$CsPbBr_{3-y}X_y$ (X = Cl, I) thin films. We studied charge-carrier dynamics of MHPs at very short times using femtosecond transient absorption spectroscopy (TAS). MHPs were deposited using spin-coating on pre-cleaned glass slides, and then the spectra were recorded in pump-probe excitation mode. TA spectra of the $CsPbBr_{3-y}X_y$ (X = Cl, I) films were recorded upon laser excitation at 390 nm (3.18 eV) at fluences of 209 and 418 μJ cm^{-2}. TA spectra of $CsPbBr_3$, excited in high energy states (*ca.* 1.36 E_g^{opt}), consist of the long-lived negative photoinduced bleach (hereafter PB), attributed to the ground state depopulation, matching with the excitonic absorption peak of MHP (520 nm), short-lived (Δt < 1 ps) positive photoinduced absorption (hereafter PA1) below the band gap (530 nm), and long-lived broad positive photoinduced absorption above the band gap (hereafter PA2) in the 460–490 nm region (Fig. 4a). Interestingly, no shoulder in the PB band was observed at early delay times originating from the biexciton effect.[43] Its absence is a characteristic of MHP bulk films,[44,45] and it can be explained here by the change in the dielectric constant of MHPs once deposited on the film, weakening coulombic forces and screening the biexciton effect.[44] We assigned the short-lived positive PA1 band to unoccupied states, slightly below the band gap, caused by band gap renormalization (BGR).[45] After Δt > 1 ps, the PA1 band vanishes simultaneously when the PA2 band arises from the shifted continuum due to BGR.[43] The temporal evolution at early delay times (up to 4 ps) for PA1, PA2, and PB band is given in Fig. 4b. The long-lived ground-state bleach is a signature of band-to-band transitions and state-filling effect.[45,46] The broadening of the bleach seems to originate from band gap renormalization (BGR), which is a consequence of the high excitation density used in our experiments.

We investigated the complex temporal evolution of the spectra at different fluences (209 and 418 μJ cm^{-2}) by a global target analysis, using a sequential kinetic model with four components (SAS) (eqn (1)).[30]

$$SAS_0 \xrightarrow{k_0} SAS_1 \xrightarrow{k_1} SAS_2 \xrightarrow{k_2} SAS_3 \quad (1)$$

SAS_0 is the instantaneous rising signal, which decays roughly within the pulse duration ($t_0 = 1/k_0 \approx 300$ fs) (Tables 1 and S3†). Since k_0 cannot be estimated with a high degree of certainty, we will focus on constants k_1 and k_2. SAS_1 appears (almost instantaneously) with the rate constant k_0 and decays with k_1. SAS_2 appears with k_1 and disappears with k_2 leading to SAS_3, which decays with k_3 ($t_3 = 1/k_3 \gg 100$ ps, *i.e.*, out of the scan range). The species-associated spectra (SAS) and the temporal evolution obtained from the global analysis are presented in Fig. S17.† The three distinctive lifetimes are attributed to the intraband cooling (t_0), state filling of the higher excitonic levels (t_1), and Auger recombination (t_2). At higher excitation fluence (418 μJ cm^{-2}) pristine $CsPbBr_3$ shows a slower relaxation (t_1 = 3.3 ps), than at the lower excitation fluence (209 μJ cm^{-2}) (t_1 = 0.77 ps) (Tables 1 and S3†). This behavior corresponds to the charge-carrier relaxation mediated through the hot-phonon bottleneck.[47] It is worth noting that such slow charge-carrier

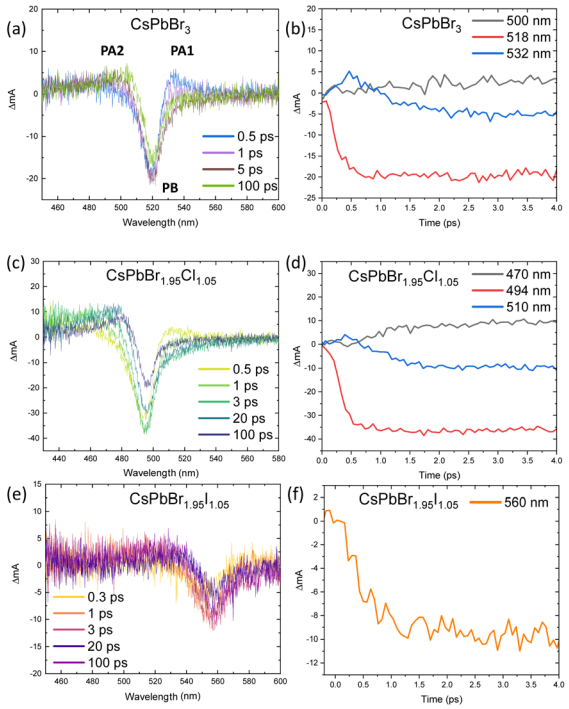

Fig. 4 (a, c and e) TA spectra, and (b, d and f) kinetics traces of $CsPbBr_3$, $CsPbBr_{1.95}Cl_{1.05}$, and $CsPbBr_{1.95}I_{1.05}$ excited at 390 nm, with a fluence of 209 μJ cm^{-2}.

relaxation could stem from polaron formation, which could also screen and reduce charge-carrier mobility, resulting in slower charge-carrier cooling dynamics.[44] Furthermore, Auger recombination lifetime, t_2, was estimated to be 52 ps and 27 ps at 209 and 418 μJ cm^{-2} excitation fluence, respectively, being in accordance with the previous reports.[48]

Anion substitution. The samples $CsPbBr_{1.65}Cl_{1.35}$ and $CsPbBr_{1.95}Cl_{1.05}$ were excited with the energy of 1.23 E_g^{opt} and 1.27 E_g^{opt}, respectively with a fluence of 209 μJ cm^{-2} (Fig. 4c, d and S19†). The presence of chloride ($CsPbBr_{1.95}Cl_{1.05}$) results in a well-pronounced blue-shifted PB band and a slower state-filling (t_1) and similar Auger recombination constant compared to pristine MHP, while excessive amount of chloride ($CsPbBr_{1.65}Cl_{1.35}$) does not contribute to the slower charge-carrier relaxation (Table 1), at this point, we can reasonably suggest that such small amounts of chloride, in $CsPbBr_{1.95}Cl_{1.05}$, reduce the density of the trapping states near the band edge, beneficial for charge-carrier relaxation. At higher excitation fluence (418 μJ cm^{-2}, Fig. S18a and b†), the presence of chloride slows down state filling effect and increases Auger recombination in both $CsPbBr_{1.65}Cl_{1.35}$ and $CsPbBr_{1.95}Cl_{1.05}$.

Our findings contrast with previous reports that demonstrate a negative effect of chloride due to the incorporation of both shallow trap states and deep ones in the conduction band.[49,50] We credit this discrepancy to the room temperature substitution method and the lower incorporated amount of chloride. Substitution with iodide significantly altered the intensity of TA spectra (Fig. 4e and S20†). The samples $CsPbBr_{1.65}I_{1.35}$ and $CsPbBr_{1.95}I_{1.05}$ were excited with the energy of 1.54 E_g^{opt} and 1.48 E_g^{opt}, respectively. In general, hole dynamics dominate iodide-based MHPs Fig. 4.[51,52]

One can observe redshift at early delay times, which is a signature of hole trapping by iodide when excited above the band gap.[52] Moreover, the PB intensity, *i.e.*, the state-filling effect, is significantly reduced due to hole trapping. In mixed $CsPbBr_{3-y}I_y$, hole transfer from bromide to iodide-rich states is energetically favored, resulting in redshifted bleach (Fig. 4e and S20a†). It was possible to monitor kinetics only at 560 nm (Fig. 4f), due to the very low intensity of PB band. At higher excitation fluence (418 μJ cm^{-2}) iodide-based perovskite showed a slower state-filling effect and enhanced Auger recombination. (Fig. S18c and d†).

From our results, we can conclude that chloride substitution reduces the density of trapping states (healing effect), especially in $CsPbBr_{1.95}Cl_{1.05}$, which is beneficial for charge-carrier relaxation to the ground state, whereas iodide act as a hole-trapping center, subjecting electrons to Auger recombination.

$CsPbBr_{3-y}X_y/TiO_2$ (X = Cl, I) thin films. We further investigated the charge-carrier dynamics of $CsPbBr_{3-y}X_y/TiO_2$ (X = Cl, I) thin films upon excitation at 209 μJ cm^{-2}. In order to limit the influence of Auger recombination, we focus only on a lower excitation fluence. Such a heterojunction demonstrated interestingly slower charge-carrier relaxation in the presence of a TiO_2 thin layer (Table 1). At this stage, we could not observe the electron transfer, but instead, in $CsPbX_3/TiO_2$ heterojunction, photogenerated excitons exhibited slightly slower charge-carrier cooling (t_1) upon anion exchange, and significantly pronounced state-filling effect (t_2) for approximately 1.3 ps for $CsPbBr_3$ and up to 3 ps for $CsPbBr_{1.65}I_{1.35}$ due to the formation of spatially indirect excitons in perovskite and TiO_2 layers (Fig. S21–S23†).[53] Interestingly, iodide-based MHPs (Fig. S23†) demonstrated a slight blue shift when coupled to a thin layer of TiO_2. The presence of TiO_2 slowed down charge-carrier cooling (t_0) and enhanced PB intensity, indicating

Table 1 Time-decay constants of $CsPbBr_{3-y}X_y$ and $CsPbBr_{3-y}X_y/TiO_2$ (X = Cl, I) thin films obtained with a global target analysis using a sequential model for the spectro-kinetics data recorded upon excitation at 390 nm with a fluence of 209 μJ cm^{-2}

Samples	t_0 (ps)	t_1 (ps)	t_2 (ps)	Samples	t_0 (ps)	t_1 (ps)	t_2 (ps)
$CsPbBr_{1.65}Cl_{1.35}$	0.26 ± 0.14	2.30 ± 0.21	25.6 ± 0.80	$CsPbBr_{1.65}Cl_{1.35}/TiO_2$	0.53 ± 0.04	5.0 ± 0.40	29.4 ± 1.6
$CsPbBr_{1.95}Cl_{1.05}$	0.42 ± 0.13	3.45 ± 0.21	47.6 ± 1.90	$CsPbBr_{1.95}Cl_{1.05}/TiO_2$	0.50 ± 0.04	4.5 ± 0.30	26.3 ± 1.1
$CsPbBr_3$	0.29 ± 0.26	0.77 ± 0.05	52.6 ± 3.15	$CsPbBr_3/TiO_2$	0.20 ± 0.02	2.1 ± 0.08	33.3 ± 1.3
$CsPbBr_{1.95}I_{1.05}$	<0.1	1.0 ± 0.02	26.3 ± 2.01	$CsPbBr_{1.95}I_{1.05}/TiO_2$	0.40 ± 0.01	3.45 ± 0.10	26.3 ± 0.5
$CsPbBr_{1.65}I_{1.35}$	0.20 ± 0.02	0.67 ± 0.05	21.7 ± 1.58	$CsPbBr_{1.65}I_{1.35}/TiO_2$	0.48 ± 0.01	3.7 ± 0.15	22.7 ± 0.5

a prolonged state-filling effect (t_1), while Auger rates (t_2) remained similar to those of $CsPbBr_{1.65}I_{1.35}$ and $CsPbBr_{1.95}I_{1.05}$ (Table 1). Such behavior could be beneficial for photocatalysis since charge accumulation does not increase Auger recombination rates.

Charge-carrier dynamics in $CsPbBr_{3-y}X_y$ and $CsPbBr_{3-y}X_y$@TiO_2 nanopowders: time-resolved photoluminescence and time-resolved microwave conductivity

To further study charge-carrier dynamics, we assessed the PL lifetime of mixed halide solid samples hybridized or not with TiO_2 (Fig. 5a and d). We observed that the used room temperature anion substitution improves PL lifetime once a small amount of Br is substituted with Cl, while a large amount of Cl induces a decrease (Fig. 5a). The average PL lifetime is estimated to be ≈ 2.42 ns for $CsPbBr_3$, increasing to ≈ 3.28 ns in $CsPbBr_{1.95}Cl_{1.05}$ and decreasing to 1.53 ns for $CsPbBr_{1.65}Cl_{1.35}$ (Table S4†). The PL lifetimes were estimated using a multi-exponential function, and it is worth noting that t_4 is of the same order of magnitude as the instrument response function. Interestingly, chloride prevents hole trapping in lead vacancies due to its high electronegativity by repulsing holes to the top of the valence band.[54] The healing effect of chloride contributes to slower thermalization due to the accumulation of the positive charges at the top valence band, in agreement with TAS measurements. In the case of iodide substitution, PL is quenched up to ≈ 0.39 ns in $CsPbBr_{1.95}I_{1.05}$, pointing out that iodide acts as a hole scavenger that translates as a non-radiative process.[54]

We further investigated charge-carrier dynamics by means of TRMC, which enables the evaluation of the charge-carrier dynamics of free electrons and holes.[55] TRMC signals obtained under UV and visible excitation (Fig. 5b and c) showed long charge-carrier lifetimes of bromide and chloride-based MHPs, exceeding μs timescale, whereas iodide-based MHPs charge-carrier lifetime does not exceed nanoscale, being in accordance with PL measurements. We complemented this study with transient photocurrent (TPC) response (to simulate natural photoactivation condition) of MHPs upon anion substitution (Fig. S24†). We observed that iodide-substituted perovskite experienced higher photocurrent response, indicating superior charge-carrier separation. We attribute this phenomenon to the holes trapped by iodide, resulting in suppressed recombination of electron–hole pairs. The photocurrent response of iodide-based perovskites exhibits a slow rise demonstrating low charge carrier mobility. This could be explained by the fast trapping of charges that is likely to screen an inner electric field and thus hinder charge transport. In contrast, $CsPbBr_3$ and chloride-based perovskites demonstrate relatively steady photocurrent responses due to shallow trapping in which electrons are captured and then slowly re-emitted.

Coating MHPs with a thin TiO_2 overlayer leads to a drastic decrease in the PL lifetime, with the average PL lifetime being below the resolution of the system (Fig. 5d), indicating electron transfer from MHP to TiO_2. TRMC signals also confirmed the electron accumulation in TiO_2 at a longer time scale (Fig. 5e and f). In the MHPs@TiO_2 nanostructures, charge-carrier dynamics is quite similar, however, the number of created charge-carrier is lower ($\Delta P/P$); we attribute this behavior to the electron

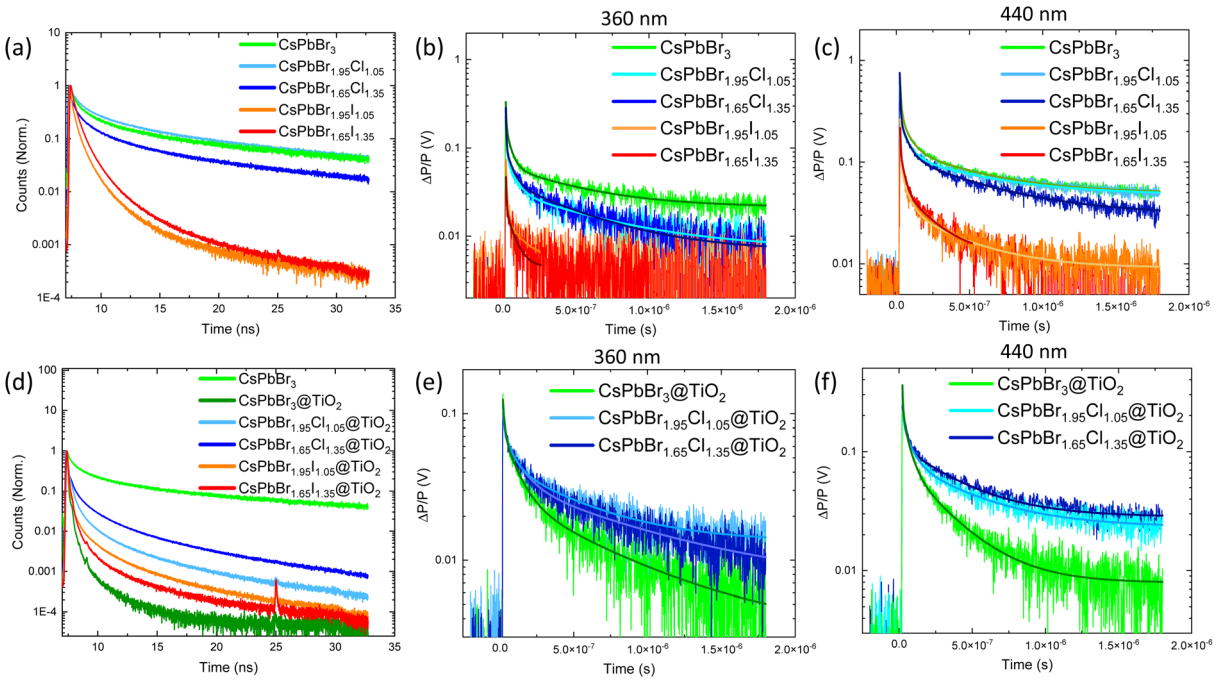

Fig. 5 TRPL lifetime decay of (a) $CsPbBr_{3-y}X_y$ and (d) $CsPbBr_{3-y}X_y$ @TiO_2 (X = Cl, I) nanostructures; TRMC signals under (b and e) UV (360 nm) and (c and f) visible (440) pulsed illumination and of $CsPbBr_{3-y}X_y$ and $CsPbBr_{3-y}X_y$ @TiO_2 (X = Cl, I) nanostructures, respectively.

screening upon the electron transfer. Interestingly, iodide-based perovskites covered by TiO_2 overlayer provide only a sharp signal (not shown), and charge-carrier lifetime decay was not observed, which is in agreement with PL lifetime analysis indicating rapid quenching at the picosecond scale. A schematic representation of the charge-carrier transfer mechanism is presented in Fig. S25† under UV (a) and visible (b) light excitation.

Photocatalytic generation of H_2 by $CsPbBr_{3-y}X_y@TiO_2$

The photocatalytic activity of the MHP@TiO_2 nanostructures was evaluated for H_2 generation in glycerol/water solution (1 : 3 v/v) under xenon lamp illumination for 3 h, and the results are shown in Fig. 6. The photocatalytic reaction of glycerol and H_2O under UV-vis illumination in the presence of a photocatalyst generates hydrogen (eqn (2) and (3)):[56]

$$C_3H_8O_3 + 3H_2O \xrightarrow{14h^+_{(VB)}} \text{intermediates} \rightarrow 3CO_2 + 14H^+ \quad (2)$$

$$14H^+ \xrightarrow{14e^-_{(CB)}} H_2(g) \quad (3)$$

MHPs alone showed fast deactivation (low stability) in aqueous solution and under light excitation compared to the composite nanostructure, observed as rapid dissolution once introduced in the glycerol/water mixture. For instance, MHPs@TiO_2 nanostructure demonstrated a stable appearance up to 3 h of photocatalytic reaction (Fig. S26†), while uncoated MHPs are dissolved after 10 min in the solution. The photocatalytic activity of pristine $CsPbBr_3@TiO_2$ demonstrated low H_2 production (Fig. 6a and b). The chloride substitution resulted in an overall decrease in the hydrogen production rate (Fig. 6b). As previously mentioned, chloride contributes to the healing defect in the valence band (VB), enhancing hole migration toward the valence band. Consequently, chloride enhances charge-carrier recombination, thus such a low H_2 production is expected. $CsPbBr_{1.95}I_{1.05}@TiO_2$ exhibit impressive hydrogen production, reaching up to 250 μmol g^{-1} after 3 h irradiation (Fig. 6b). Since iodide acts as a hole trapper, it inhibits charge carrier recombination, allowing more electrons in the conduction band (CB) to be available for proton reduction. Moreover, the fast electron transfer to TiO_2 and hole injection from TiO_2 to VB of perovskites contributes to the enhancement of interfacial charge separation, which is beneficial for the H_2 generation. However, larger iodide amount in $CsPbBr_{1.65}I_{1.35}@TiO_2$ does not lead to a further enhancement of H_2 evolution, probably due to increased hole trapping centers that cannot be compensated with hole injection from TiO_2 (Fig. 6b). The optimal photocatalytic H_2 evolution reaction is obtained with $CsPbBr_{1.95}I_{1.05}@TiO_2$, showing an optimal interfacial charge-carrier separation.

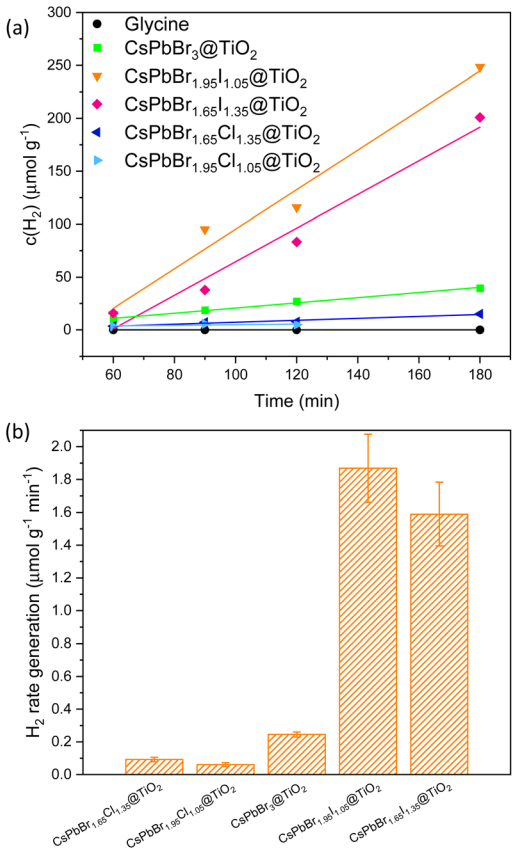

Fig. 6 (a) Photocatalytic activity and (b) H_2 evolution rate of the MHP@TiO_2 nanostructures.

Conclusions

In this work, we demonstrated room temperature anion substitution in $CsPbBr_3$ nanocrystals, that yields stable highly emissive mixed halide Cl/Br perovskites and low emissive orthorhombic mixed halide I/Br perovskites. A room temperature method offers a possibility of defect healing through the addition of small amounts of chloride, directly influencing the enhancement of photoluminescence lifetime. However, the addition of iodide results in the formation of hole-trapping centers that prevent radiative charge-carrier recombination. We further investigated the electron transfer from metal-halide perovskite to TiO_2. Ultrafast charge carrier dynamics (TAS) proved slower charge carrier relaxation due to the formation of indirect excitons between MHPs and the TiO_2 layer, which is significantly pronounced in $CsPbBr_{1.95}I_{1.05}/TiO_2$ and $CsPbBr_{1.65}I_{1.35}/TiO_2$ thin films. $CsPbBr_{1.95}I_{1.05}@TiO_2$ demonstrated the highest photocatalytic hydrogen production, owing to electron transfer to TiO_2 and hole injection from TiO_2 to $CsPbBr_{1.95}I_{1.05}$, essential for water splitting. These results represent a step forward in hydrogen generation from aqueous solutions.

Author contributions

M. K. performed the experiments, curated the data, and wrote the first draft of the ms. V.-D. Q. carried out and discussed the electrochemical measurements and characterizations. I. L. discussed the TAS results. D. B. performed and discussed the XRD results. P. P. helped curating the TAS data. M. E. performed

the TRPL analysis and discussed the results. C. C.-J. discussed the work. M. N. G. conceived and supervised the work. The manuscript was written through contributions of all authors.

Conflicts of interest

There are no conflicts to declare.

Acknowledgements

MK acknowledges the French "Ministère de l'enseignement supérieur et de la recherche" (MESR) for the PhD Grant. MNG thanks the public grant overseen by the French National Research Agency (ANR), through the IngenCat project (ANR-20-CE43-0014), and NEXTCCUS project as part of the ERANET-ACT3 call program for the financial support. The authors thank François Brisset for his valuable help in performing STEM and TEM analysis.

References

1 R. A. Scheidt, E. Kerns and P. V. Kamat, *J. Phys. Chem. Lett.*, 2018, **9**, 5962–5969.
2 **https://www.nrel.gov/pv/cell-efficiency.html**.
3 J. Li, L. Wang, X. Yuan, B. Bo, H. Li, J. Zhao and X. Gao, *Mater. Res. Bull.*, 2018, **102**, 86–91.
4 K. Su, G. X. Dong, W. Zhang, Z. L. Liu, M. Zhang and T. B. Lu, *ACS Appl. Mater. Interfaces*, 2020, **12**, 50464–50471.
5 Y. F. Xu, M. Z. Yang, B. X. Chen, X. D. Wang, H. Y. Chen, D. Bin Kuang and C. Y. Su, *J. Am. Chem. Soc.*, 2017, **139**, 5660–5663.
6 Y. F. Xu, X. D. Wang, J. F. Liao, B. X. Chen, H. Y. Chen and D. Bin Kuang, *Adv. Mater. Interfaces*, 2018, **5**, 1801015.
7 Z. Y. Chen, Q. L. Hong, H. X. Zhang and J. Zhang, *ACS Appl. Energy Mater.*, 2022, **5**, 1175–1182.
8 Z. C. Kong, J. F. Liao, Y. J. Dong, Y. F. Xu, H. Y. Chen, D. Bin Kuang and C. Y. Su, *ACS Energy Lett.*, 2018, **3**, 2656–2662.
9 L. Li, Z. Zhang, C. Ding and J Xu, *Chem. Eng. J.*, 2021, **419**, 129543.
10 Z. Zhang, M. Shu, Y. Jiang and J. Xu, *Chem. Eng. J.*, 2021, **414**, 128889.
11 A. Pan, X. Ma, S. Huang, Y. Wu, M. Jia, Y. Shi, Y. Liu, P. Wangyang, L. He and Y. Liu, *J. Phys. Chem. Lett.*, 2019, **10**, 6590–6597.
12 M. Ou, W. Tu, S. Yin, W. Xing, S. Wu, H. Wang, S. Wan, Q. Zhong and R. Xu, *Angew. Chem., Int. Ed.*, 2018, **57**, 13570–13574.
13 W. Song, Y. Wang, C. Wang, B. Wang, J. Feng, W. Luo, C. Wu, Y. Yao and Z. Zou, *ChemCatChem*, 2021, **13**, 1711–1716.
14 R. Tang, S. Zhou, H. Li, R. Chen, L. Zhang and L. Yin, *Appl. Catal., B*, 2020, **265**, 118583.
15 K. Gu, Y. Wang, J. Shen, J. Zhu, Y. Zhu and C. Li, *ChemSusChem*, 2020, **13**, 682–687.
16 Z. Chen, Y. Hu, J. Wang, Q. Shen, Y. Zhang, C. Ding, Y. Bai, G. Jiang, Z. Li and N. Gaponik, *Chem. Mater.*, 2020, **32**, 1517–1525.
17 Z. C. Kong, H. H. Zhang, J. F. Liao, Y. J. Dong, Y. Jiang, H. Y. Chen and D. Bin Kuang, *Sol. RRL*, 2020, **4**, 1900365.
18 L. Zhou, *Theory Model. Dispersed Multiph. Turbul. React. Flows*, 2018, pp. 15–70.
19 S.-H. Guo, J. Zhou, X. Zhao, C.-Y. Sun, S.-Q. You, X.-L. Wang and Z.-M. Su, *J. Catal.*, 2019, **369**, 201–208.
20 Y. Xu, W. Zhang, K. Su, Y. X. Feng, Y. F. Mu, M. Zhang and T. B. Lu, *Chem.–Eur. J.*, 2021, **27**, 2305–2309.
21 Y. Li, Q. Shu, Q. Du, Y. Dai, S. Zhao, J. Zhang, L. Li and K. Chen, *ACS Appl. Mater. Interfaces*, 2020, **12**, 451–460.
22 S. Shyamal, S. K. Dutta, T. Das, S. Sen, S. Chakraborty and N. Pradhan, *J. Phys. Chem. Lett.*, 2020, **11**, 3608–3614.
23 S. Shyamal, S. K. Dutta and N. Pradhan, *J. Phys. Chem. Lett.*, 2019, **10**, 7965–7969.
24 Y. W. Liu, S. H. Guo, S. Q. You, C. Y. Sun, X. L. Wang, L. Zhao and Z. M. Su, *Nanotechnology*, 2020, **31**, 215605.
25 Y. F. Mu, W. Zhang, X. X. Guo, G. X. Dong, M. Zhang and T. B. Lu, *ChemSusChem*, 2019, **12**, 4769–4774.
26 L. Ding, C. Shen, Y. Zhao, Y. Chen, L. Yuan, H. Yang, X. Liang, W. Xiang and L. Li, *Mol. Catal.*, 2020, **483**, 1–7.
27 L. Protesescu, S. Yakunin, M. I. Bodnarchuk, F. Krieg, R. Caputo, C. H. Hendon, R. X. Yang, A. Walsh and M. V. Kovalenko, *Nano Lett.*, 2015, **15**, 3692–3696.
28 C. Lu, M. W. Wright, X. Ma, H. Li, D. S. Itanze, J. A. Carter, C. A. Hewitt, G. L. Donati, D. L. Carroll, P. M. Lundin and S. M. Geyer, *Chem. Mater.*, 2019, **31**, 62–67.
29 N. M. Ghazzal, N. Chaoui, E. Aubry, A. Koch and D. Robert, *J. Photochem. Photobiol., A*, 2010, **215**, 11–16.
30 P. Pernot, SK-ana, 2018, DOI: **10.5281/zenodo.1064370**.
31 C. Ruckebusch, M. Sliwa, P. Pernot, A. de Juan and R. Tauler, *J. Photochem. Photobiol., C*, 2012, **13**, 1–27.
32 I. H. M. Van Stokkum, D. S. Larsen and R. Van Grondelle, *Biochim. Biophys. Acta, Bioenerg.*, 2004, **1657**, 82–104.
33 M. Erard, A. Fredj, H. Pasquier, D. B. Beltolngar, Y. Bousmah, V. Derrien, P. Vincent and F. Merola, *Mol. BioSyst.*, 2013, **9**, 258–267.
34 G. D. Gesesse, C. Li, E. Paineau, Y. Habibi, H. Remita, C. Colbeau-Justin and M. N. Ghazzal, *Chem. Mater.*, 2019, **31**, 4851–4863.
35 C. Wang, J. Li, E. Paineau, A. Laachachi, C. Colbeau-Justin, H. Remita and M. N. Ghazzal, *J. Mater. Chem. A*, 2020, **8**, 10779–10786.
36 G. Nedelcu, L. Protesescu, S. Yakunin, M. I. Bodnarchuk, M. J. Grotevent and M. V. Kovalenko, *Nano Lett.*, 2015, **15**, 5635–5640.
37 M. V. Kovalenko, L. Protesescu and M. I. Bodnarchuk, *Science*, 2017, **358**, 745–750.
38 S. N. Inamdar, P. P. Ingole and S. K. Haram, *ChemPhysChem*, 2008, **9**, 2574–2579.
39 S. K. Haram, B. M. Quinn and A. J. Bard, *J. Am. Chem. Soc.*, 2001, **123**, 8860–8861.
40 F. Liu, C. Ding, Y. Zhang, T. S. Ripolles, T. Kamisaka, T. Toyoda, S. Hayase, T. Minemoto, K. Yoshino, S. Dai, M. Yanagida, H. Noguchi and Q. Shen, *J. Am. Chem. Soc.*, 2017, **139**, 16708–16719.

41 Z. Dang, J. Shamsi, F. Palazon, M. Imran, Q. A. Akkerman, S. Park, G. Bertoni, M. Prato, R. Brescia and L. Manna, *ACS Nano*, 2017, **11**, 2124–2132.
42 Z. J. Li, E. Hofman, J. Li, A. H. Davis, C. H. Tung, L. Z. Wu and W. Zheng, *Adv. Funct. Mater.*, 2018, **28**, 1704288.
43 A. Mondal, J. Aneesh, V. Kumar Ravi, R. Sharma, W. J. Mir, M. C. Beard, A. Nag and K. V Adarsh, *Phys. Rev. B*, 2018, **98**, 115418.
44 G. Kaur and H. N. Ghosh, *J. Phys. Chem. Lett.*, 2020, **11**, 8765–8776.
45 J. Butkus, P. Vashishtha, K. Chen, J. K. Gallaher, S. K. K. Prasad, D. Z. Metin, G. Laufersky, N. Gaston, J. E. Halpert and J. M. Hodgkiss, *Chem. Mater.*, 2017, **29**, 3644–3652.
46 J. Aneesh, A. Swarnkar, V. Kumar Ravi, R. Sharma, A. Nag and K. V Adarsh, *J. Phys. Chem. C*, 2017, **121**, 4734–4739.
47 A. Mondal, J. Aneesh, V. Kumar Ravi, R. Sharma, W. J. Mir, M. C. Beard, A. Nag and K. V. Adarsh, *Phys. Rev. B*, 2018, **98**, 115418.
48 A. Mondal, J. Aneesh, V. Kumar Ravi, R. Sharma, W. J. Mir, M. C. Beard, A. Nag and K. V. Adarsh, *Phys. Rev. B*, 2018, **98**, 115418.
49 N. Soetan, A. Puretzky, K. Reid, A. Boulesbaa, H. F. Zarick, A. Hunt, O. Rose, S. Rosenthal, D. B. Geohegan and R. Bardhan, *ACS Photonics*, 2018, **5**, 3575–3583.
50 S. Mandal, S. Ghosh, S. Mukherjee, C. K. De, D. Roy, T. Samanta and P. K. Mandal, *Nanoscale*, 2021, **13**, 3654–3661.
51 H. Chung, S. Il Jung, H. J. Kim, W. Cha, E. Sim, D. Kim, W.-K. Koh and J. Kim, *Angew. Chem., Int. Ed.*, 2017, **56**, 4160–4164.
52 N. Mondal and A. Samanta, *Nanoscale*, 2017, **9**, 1878–1885.
53 Z. Gevorkian, V. Gasparian and Y. Lozovik, *Appl. Phys. Lett.*, 2016, **108**, 51109.
54 G. Nan, X. Zhang, M. Abdi-Jalebi, Z. Andaji-Garmaroudi, S. D. Stranks, G. Lu and D. Beljonne, *Adv. Energy Mater.*, 2018, **8**, 1–9.
55 E. M. Hutter and T. J. Savenije, *ACS Energy Lett.*, 2018, **3**, 2068–2069.
56 V. Kumaravel, M. D. Imam, A. Badreldin, R. K. Chava, J. Y. Do, M. Kang and A. Abdel-Wahab, *Catal*, 2019, **9**, 276.

